WIND-BLOWN SAND EROSION OF A POLYCARBONATE LAMP COVER FOR AGRICULTURAL MACHINERY AT DIFFERENT WIND SPEEDS AND YAW ANGLES

/

不同风速与偏航角下农用机械聚碳酸酯灯罩的风沙冲蚀特性

Sheng JIANG, Afang JIN*), Mengyao XU
College of Mechanical Engineering, Xinjiang University, Urumqi 830046/ China;
Tel: +86-17591715179; E-mail: jinaf3500@163.com
DOI: https://doi.org/10.35633/inmateh-79-90

Keywords: *agricultural-machinery lamp cover, wind-blown sand erosion, yaw angle, Eulerian–Lagrangian approach, polycarbonate*

ABSTRACT

Wind-blown sand erosion threatens agricultural-vehicle lamp covers, yet the effects of wind speed and yaw angle have not been sufficiently quantified. A one-way coupled Eulerian–Lagrangian CFD model of a full-scale isolated polycarbonate (PC) lamp cover was combined with gas-jet erosion tests on flat PC specimens for trend-level comparison. Wind speeds of 10–30 m/s and yaw angles of −30° to 30° were investigated, with erosion predicted using the Oka model. Erosion was concentrated near the windward leading edge and downstream surface, whereas the maximum pressure remained closer to the stagnation region. The mean and maximum erosion rates followed power-law relationships with exponents of 2.70 and 2.31, respectively. From −30° to 30°, the mean erosion rate increased by 28.3%, 57.0%, and 13.9% at 10, 20, and 30 m/s, respectively. At 30 m/s, the maximum erosion rate increased by 55.8% from 0° to 30°. At 20 m/s, the erosion concentration factors were 13.31, 5.45, and 9.54 at −30°, 0°, and 30°, respectively. Over the same yaw-angle range, the experimental mass loss increased by 212.5%, 115.4%, and 88.9%, while the surface roughness increased by 23.9%, 18.9%, and 20.1%. After normalization, the numerical and experimental indicators exhibited consistent yaw-angle-dependent trends (R^2 = 0.9481, RMSE = 0.0822, MAE = 0.0671). Within the investigated conditions, the model successfully captured the relative erosion trends, and the combined indicators supported the assessment of localized erosion risk.

摘要

风沙冲蚀对农用车辆灯罩的服役性能构成威胁，但风速与偏航角对其冲蚀特性的影响尚未得到充分量化。本文建立全尺寸孤立灯罩的单向耦合欧拉–拉格朗日 CFD 模型，并结合平板聚碳酸酯试样气固射流冲蚀试验进行趋势对比。研究考虑 10–30 m/s 的风速和−30°–30°的偏航角，并采用 Oka 模型预测冲蚀。结果表明，冲蚀主要集中于迎风前缘及其下游表面，而压力峰值更接近滞止区域。平均冲蚀率和最大冲蚀率均与风速呈幂律关系，其指数分别为 2.70 和 2.31。偏航角由−30°增至 30°时，10、20 和 30 m/s 下的平均冲蚀率分别增加 28.3%、57.0% 和 13.9%。在 30 m/s 下，最大冲蚀率由 0°至 30°增加 55.8%。在 20 m/s 下，−30°、0°和 30°对应的冲蚀集中系数分别为 13.31、5.45 和 9.54。在相同偏航角范围内，试验质量损失分别增加 212.5%、115.4%和 88.9%，表面粗糙度分别增加 23.9%、18.9%和 20.1%。归一化后的数值与试验指标均呈现出一致的偏航角依赖变化规律。（R^2 = 0.9481，RMSE = 0.0822，MAE = 0.0671）。在本文研究条件下，该模型能够反映相对冲蚀变化趋势，综合指标可为局部冲蚀风险评估提供依据。

INTRODUCTION

Modern agricultural machinery is widely used for crop production, land reclamation, and material transport in arid, semi-arid, and desertified agricultural regions, where near-ground flows frequently contain wind-blown sand and dust particles *(Li et al., 2025; Yan et al., 2024)*. These particles are transported mainly through saltation and suspension, and their motion is governed by wind velocity, turbulence intensity, surface roughness, and particle inertia *(Kok et al., 2012; Shao and Lu, 2000)*. During field operation, vehicle motion and crosswinds may generate stagnation, acceleration, and flow-separation regions around frontal surfaces, thereby modifying particle trajectories, impact velocity, and local incidence conditions. Repeated particle impacts on exposed transparent components may consequently cause pits, scratches, material loss, and progressive optical degradation *(Zhao et al., 2021)*.

Solid-particle erosion is a surface-degradation process governed by particle kinetic energy, impact angle, and material response. Its principal damage modes include cutting, ploughing, plastic deformation, and localized fracture *(Bellman and Levy, 1981; Deng, 2025; Finnie, 1960; Hutchings, 1981; Sundararajan, 1991)*, while erosion severity is influenced by impact velocity, particle characteristics, and material toughness. For agricultural-machinery lamp covers, wind-blown sand erosion may lead to material removal, surface roughening, haze formation, and reduced light transmittance, thereby affecting illumination range and field-boundary recognition during night-time or dusty operation. Failure analyses of automotive headlamp lenses have also shown that surface degradation and cracking may compromise the functional integrity of transparent lighting components *(Ferreira and Lins, 2019)*. Polycarbonate (PC) is widely used for transparent vehicle components because of its optical transparency, low weight, and impact resistance *(Katsamberis et al., 1998)*. Its erosion response is closely associated with resilience, impact-energy absorption, and local deformation under repeated particle impacts *(Xie et al., 2019)*. The gradual accumulation of pits, grooves, and scratches may therefore alter both the surface condition and optical performance of PC lamp covers exposed to wind-blown sand.

Previous studies of wind-blown sand and solid-particle erosion have focused mainly on turbomachinery components and wind-turbine blades *(Alqallaf et al., 2020; Hamed et al., 2006; Wang et al., 2024)*. These studies show that wind velocity, particle mass flow rate, particle characteristics, and wall impact angle strongly influence erosion location and intensity, providing a basis for understanding particle transport and wall collision in gas–solid flows *(Deng, 2025)*. However, curved transparent components on agricultural machinery exhibit different geometrical boundaries and local flow conditions. Under yawed wind-blown sand inflow, changes in the incoming-flow direction redistribute the velocity field, pressure gradient, particle concentration, and impact-angle distribution around the lamp cover. The resulting variation in the position, intensity, and spatial concentration of high-erosion regions therefore requires further quantitative analysis.

Eulerian–Lagrangian and CFD–DEM approaches have been applied to gas–particle transport in agricultural equipment and aeolian-sand systems *(Bi et al., 2023; Chen et al., 2025; Li et al., 2025; Zhang et al., 2025)*. These methods enable particle trajectories, impact conditions, and erosion distributions to be evaluated under controlled operating conditions. However, mean erosion alone cannot fully characterize local peak damage, particularly when erosion becomes spatially concentrated under yawed inflow. Therefore, both overall erosion severity and localized erosion characteristics should be considered when assessing the erosion risk of exposed transparent components.

The objectives of this study are to: (1) establish a one-way coupled Eulerian–Lagrangian framework for predicting wind-blown sand transport and erosion on a full-scale isolated agricultural-machinery lamp cover; (2) quantify the effects of wind speed and yaw angle on the mean erosion rate, maximum erosion rate, and erosion concentration factor; (3) identify variations in erosion-prone regions and the spatial concentration of erosion under different operating conditions; and (4) conduct gas-jet erosion tests on flat PC coupons to determine whether mass loss, surface roughness, and surface morphology follow the parametric trends predicted numerically.

MATERIALS AND METHODS

Numerical simulation

Governing Equations and Numerical Models

A one-way coupled Eulerian–Lagrangian CFD model was developed to simulate air–sand two-phase flow around an agricultural-machinery lamp cover under wind-blown sand conditions. The airflow was solved as a continuous phase using the Reynolds-averaged Navier–Stokes equations, while sand-particle trajectories were tracked in a Lagrangian framework. Owing to the low particle volume fraction, particle feedback on the airflow was neglected *(Elghobashi, 1994)*. The SST k–ω model was adopted to account for adverse pressure gradients and flow separation near the curved lamp-cover surface *(Menter, 1994)*. Identical numerical schemes and convergence criteria were applied to all wind-speed and yaw-angle cases to ensure consistent comparison.

After convergence of the continuous-phase solution, the sand-particle trajectories were calculated. Interparticle collisions were neglected, and the particle equation of motion was formulated according to Newton's second law:

$$m_p \frac{d\mathbf{v}_p}{dt} = \mathbf{F}_D + m_p\mathbf{g} + \mathbf{F}_{other} \tag{1}$$

where m_p is the particle mass, $\boldsymbol{v}_p$ is the particle velocity vector, $\boldsymbol{F}_D$ is the drag force exerted by the fluid on the particle, and $\boldsymbol{F}_{\text{other}}$ includes the pressure-gradient force and Saffman lift force. The drag force was determined from the local relative velocity, particle Reynolds number, and drag coefficient.

Material loss caused by particle impact was evaluated using the Oka erosion model *(Oka et al., 1997; Oka et al., 2005a; Oka and Yoshida, 2005b)*. In the model, the erosion ratio is determined by the particle impact angle, impact velocity, particle diameter, and material-related coefficients:

$$E(\alpha, V_p, d_p) = E_{\mathrm{ref}}\, g(\alpha)\left(\frac{V_p}{V_{\mathrm{ref}}}\right)^{k_v}\left(\frac{d_p}{d_{\mathrm{ref}}}\right)^{k_d} \tag{2}$$

The impact-angle correction function is expressed as:

$$g(\alpha) = (\sin\,\alpha)^{n_1}[1 + H_v(1 - \sin\,\alpha)]^{n_2} \tag{3}$$

where $E(\alpha, V_p, d_p)$ is the ratio of eroded material mass to incident particle mass; E_{ref} is the reference erosion ratio; $g(\alpha)$ is the impact-angle correction function; and α is the particle impact angle. V_p and d_p denote the particle velocity immediately before wall impact and the particle diameter, respectively, whereas V_{ref} and d_{ref} are the corresponding reference values. H_v is the hardness coefficient used in the Oka model, n_1 and n_2 are the impact-angle coefficients, and k_v and k_d are the velocity and diameter exponents, respectively.

The parameters used in the simulations are listed in Table 1. The reference erosion ratio was 2.141×10^{-4}, while the reference velocity and particle diameter were 104 m/s and 3.26×10^{-4}m, respectively. The hardness coefficient was 1.34, resulting in impact-angle coefficients $n_1 = 0.7397$ and $n_2 = 1.8228$. The velocity and diameter exponents were 2.3257 and 0.19, respectively. The same parameter set was applied to all wind-speed and yaw-angle conditions, without case-specific adjustment.

Table 1

Parameters used in the Oka erosion model

Parameter	Symbol	Value	Unit
Reference erosion ratio	E_{ref}	2.141×10^{-4}	-
Hardness coefficient	H_v	1.34	-
Impact-angle coefficient	n_1	0.7397	-
Impact-angle coefficient	n_2	1.8228	-
Reference velocity	V_{ref}	104	m/s
Velocity exponent	k_v	2.3257	-
Reference particle diameter	d_{ref}	326	μm
Diameter exponent	k_d	0.19	-

Note: *$d_{ref} = 326\,\mu m$ is the reference diameter in the Oka model, whereas the actual particle diameters followed a log-normal distribution within the specified particle-size range.*

The default Oka-model parameter set was used without independent calibration for the present quartz-sand–PC system. Therefore, the calculated erosion rates were used primarily to compare spatial distributions and relative variations among operating conditions rather than to predict absolute material loss.

The local erosion rate was calculated from the particle mass flow rates associated with the trajectories striking each wall-face cell:

$$\dot{m}''_{\mathrm{e},f} = \frac{1}{A_f}\sum_{j=1}^{N_f} E(\alpha_j)\dot{m}_{\mathrm{p},j} \tag{4}$$

where $\dot{m}''_{e,f}$ is the erosion rate of the f-th wall-face cell, A_f is the area of the cell, N_f is the number of particle trajectories striking the cell; and $\dot{m}_{p,j}$ is the mass flow rate represented by the j-th particle trajectory.

The mean and maximum erosion rates over the lamp-cover surface are defined as:

$$\dot{m}''_{e,\mathrm{avg}} = \frac{\sum_{f=1}^{N}\dot{m}''_{e,f}A_f}{\sum_{f=1}^{N}A_f}, \dot{m}''_{e,\mathrm{max}} = \max_{1\le f\le N}\left(\dot{m}''_{e,f}\right) \tag{5}$$

where $\dot{m}''_{e,\mathrm{avg}}$ and $\dot{m}''_{e,\mathrm{max}}$ denote the mean and maximum erosion rates, respectively, and N is the total number of wall-face cells on the agricultural vehicle lamp cover. The mean erosion rate characterizes the overall material loss from the lamp-cover surface, whereas the maximum erosion rate reflects the severity of localized erosion. These two parameters are used to evaluate the overall erosion level and local damage concentration under different wind-speed and yaw-angle conditions.

Geometric Model and Computational Domain

A three-dimensional model of a representative **PC lamp cover used on agricultural machinery** was constructed to investigate its wind-blown sand erosion characteristics. The external contour and curvature of the exposed lamp-cover surface were retained, whereas mounting structures and internal optical components were omitted. The adjacent body panels, grille, bumper, and other surrounding vehicle structures were not included; therefore, the lamp cover was treated as an isolated component in the computational domain. The resulting model had overall dimensions of approximately 415 mm × 431 mm × 201 mm.

Because the surrounding vehicle body was excluded, the calculated results represent the aerodynamic and erosion responses of the isolated lamp cover and are primarily applicable to comparative analyses of wind speed and yaw angle.

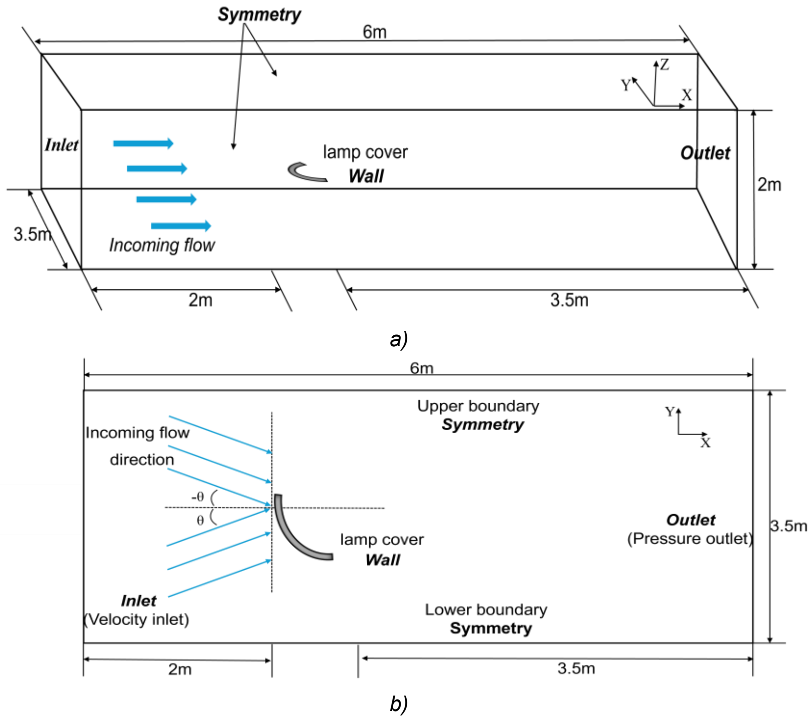

Fig. 1 - Schematic of the computational domain

a) three-dimensional computational domain; b) top view and definition of the yaw angle

As shown in Figure 1(a), the computational domain extended 2 m upstream and 3.5 m downstream of the lamp cover, with overall dimensions of 6 m × 3.5 m × 2 m. This arrangement limited the blockage ratio to less than 3% and reduced the influence of the outer boundaries on the flow around the lamp cover. The inlet and outlet were specified as a velocity inlet and a pressure outlet, respectively, while the remaining outer boundaries were treated as symmetry boundaries.

The yaw angle θ was defined as the angle between the incoming-flow direction and the central normal axis of the lamp cover, as illustrated in Figure 1(b). Five yaw-angle conditions, −30°, −15°, 0°, 15°, and 30°, were considered. A Cartesian coordinate system was adopted, with the X-axis aligned was aligned with the inflow direction at the 0° reference condition, the Y-axis oriented transversely, and the Z-axis directed vertically. Different yaw conditions were imposed by rotating the inlet velocity vector while keeping the computational domain unchanged.

Mesh Generation and Grid Sensitivity Verification

The computational domain was discretized using polyhedral cells, which are well suited to the curved lamp-cover surface and its surrounding flow field. Prism layers were generated along the lamp-cover wall to resolve the near-wall flow. The boundary-layer mesh consisted of 15 layers with a total thickness of 5 mm and a growth rate of 1.2. Local refinement was applied to the windward surface, regions of pronounced curvature, and areas expected to experience high erosion. This mesh arrangement provided sufficient resolution of the near-wall flow and particle impacts without imposing excessive computational cost.

Grid sensitivity was examined using three meshes under a wind speed of 20 m/s, a particle mass flow rate of 2 g·s^{-1}, and a yaw angle of 0°. As reported in Table 2, increasing the cell count from 0.68×10^6 to 1.24×10^6 changed the mean and maximum erosion rates by 2.22% and 2.37%, respectively. Further refinement to 1.83×10^6 cells reduced the corresponding changes to 0.72% and 1.04%. The medium and fine meshes therefore produced closely comparable results, with all variations remaining below 5%. Considering both numerical accuracy and computational cost, the mesh containing 1.24×10^6 cells was selected for the subsequent simulations.

Table 2

Results of the grid-independence study

Number of cells (10^6)	Mean erosion rate (10^{-9} kg·m^{-2}·s^{-1})	Variation (%)	Maximum erosion rate (10^{-9} kg·m^{-2}·s^{-1})	Variation (%)
0.68	1.35	--	7.58	--
1.24	1.38	2.22	7.76	2.37
1.83	1.39	0.72	7.84	1.04

Gas-Jet Sand Erosion Experiment

Gas-jet sand erosion tests were conducted to examine the effects of wind speed and specimen orientation on the mass loss, surface roughness, and surface morphology of PC coupons, and to compare the resulting parametric trends with the numerical predictions *(ASTM International, 2018)*. As shown in Figure 2(a), the test system comprised an air compressor, a pressure regulator, an abrasive feed unit, a nozzle, a specimen rotation stage, and a material recovery chamber. Compressed air entered the nozzle after pressure regulation, where quartz sand particles were entrained and accelerated by the high-speed airflow. The particles then struck the specimen at the prescribed velocity and orientation. The rotation stage controlled the specimen position and yaw angle, while the recovery chamber collected the particles after impact. Surface morphology and local roughness after erosion were examined using the digital microscope shown in Figure 2(b).

a) *b)*

Fig. 2 - Experimental instruments

a) wind–sand erosion test system; b) extended-depth-of-field imaging system.

To introduce an asymmetric reference orientation comparable with the installed lamp cover in its installed position, the specimen was mounted with an initial nozzle angle of α_0=15°. The distance from the nozzle outlet to the specimen center was fixed at $S = 200$ mm, as illustrated in Figure 3. The 0° yaw condition corresponded to the installation reference position rather than normal impact. With α_0 held constant, the specimen rotation stage was adjusted to obtain yaw angles of −30°, −15°, 0°, 15°, 30°. The same nominal yaw-angle range was used in the numerical and experimental cases to facilitate trend comparison.

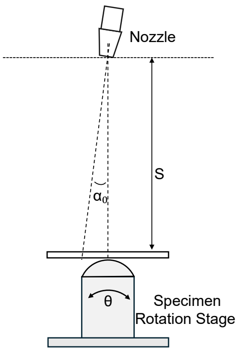

Fig. 3 - Initial nozzle orientation and definition of the specimen yaw angle

The principal test conditions are listed in Table 3. PC specimens were eroded by quartz sand at nominal nozzle-exit air velocity of 10, 20, and 30 m/s. Each test lasted 60 s and was independently repeated three times. Specimen mass was measured before and after erosion using an analytical balance with a resolution of 0.001 g. The measured mass loss, surface roughness, and surface morphology were used to compare the effects of wind speed and yaw angle with the corresponding numerical trends.

Table 3

Experimental conditions for gas-jet sand erosion tests

Parameter	Value
Specimen material	Polycarbonate (PC)
Specimen size	40 mm × 40 mm × 3 mm
Particle material	Quartz sand
Particle density	2650 kg/m^3
Particle size	50–250 μm
Nozzle inner diameter, D_n	6 mm
Sand mass flow rate, $\dot{m}_s$	2.5 g/s
Nominal air velocity	10, 20, and 30 m/s
Initial nozzle angle, α_0	15°
Yaw angle, θ	−30°, −15°, 0°, 15° and 30°
Nozzle–specimen distance, S	200 mm
Exposure time	60 s
Number of repetitions	3

RESULTS

Numerical simulation results and analysis

Effect of Yaw Angle on Surface Erosion and Pressure Distributions

Figure 4 compares the surface erosion-rate and pressure distributions on the agricultural-machinery lamp cover at 20 m/s under different yaw angles. As shown in Figure 4(a), erosion was mainly concentrated near the windward leading edge and the adjacent downstream surface, whereas the leeward region remained at a relatively low erosion level. As the yaw angle changed from −30° to 30°, the high-erosion region gradually expanded, while its main location remained near the windward leading edge. This distribution is associated with particle inertia in the curved flow. Because particles cannot instantaneously follow strongly turning streamlines, they may retain wall-directed momentum and impact the windward region. A similar dependence of wind-sand transport on local flow-field modification was reported by *Yan et al., (2024)*.

The pressure contours in Figure 4(b) show a maximum near the windward stagnation region, followed by a downstream decrease. Although the pressure and erosion distributions partially correspond, the erosion peak is located slightly downstream of the pressure maximum. This offset reflects the different dynamics of the gas and particle phases: pressure is governed by gas-phase stagnation, whereas erosion depends on particle impact velocity and angle. Particle inertia may therefore shift the strongest impact away from the pressure peak. This interpretation is consistent with *Oka et al., (2005a)*, who identified impact velocity and impact angle as key parameters controlling solid-particle erosion.

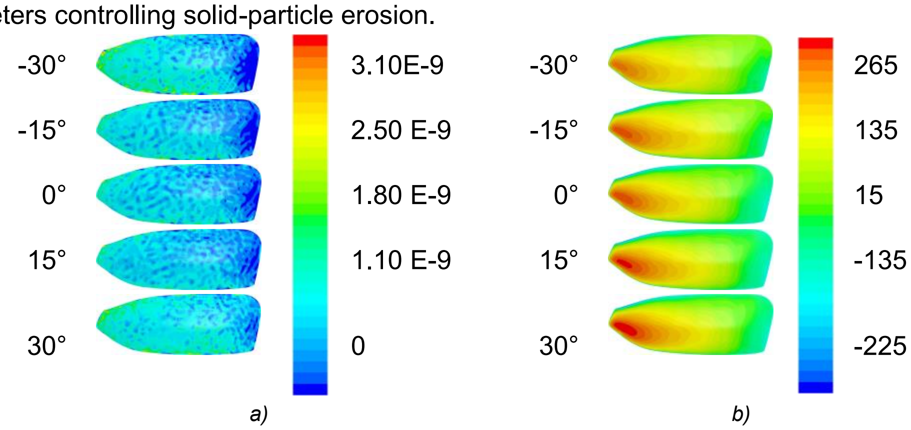

Fig. 4 - Surface erosion-rate and gauge-pressure distributions at 20 m/s under different yaw angles

a) Erosion rate distribution (kg·m^{-2}·s^{-1}); b) surface gauge-pressure distribution (Pa)

Effects of Wind Speed and Yaw Angle on Erosion Characteristics

Figure 5 shows that increasing wind speed markedly intensified surface erosion on the agricultural vehicle lamp cover, whereas yaw angle mainly changed the spatial distribution of erosion on the curved surface. As shown in Figure 5(a), the mean erosion rate generally increased as the yaw angle changed from −30° to 30° at the same wind speed, with increases of 28.3%, 57.0%, and 13.9% at 10, 20, and 30 m/s, respectively.

Higher wind speed increases particle impact velocity and energy transfer, thereby increasing the overall erosion magnitude, which reached its highest level at 30 m/s. In contrast, yaw modifies particle trajectories and incidence conditions, and its relative influence was most pronounced at 20 m/s. This non-monotonic yaw sensitivity may arise from the combined effects of particle-impact intensity and yaw-induced trajectory redistribution. This result is similar to *Li et al., (2025)*, who identified wind speed as a dominant factor in aeolian-particle transport.

As shown in Fig. 5(b), the mean erosion rate increased with wind speed according to a power-law relationship with an exponent of approximately 2.70. This velocity dependence is consistent with the Oka erosion model, indicating that the fitted exponent characterizes the velocity sensitivity of the present flow–particle–erosion system rather than representing an intrinsic material constant of PC.

In contrast to the mean erosion rate, Fig. 5(c) shows an approximately U-shaped variation in the maximum erosion rate with yaw angle. At 30 m/s, the maximum erosion rate increased from approximately 2.13×10^{-8} kg·m^{-2}·s^{-1} at 0° to 3.33×10^{-8} kg·m^{-2}·s^{-1} at 30°, corresponding to an increase of approximately 56%. Figure 5(d) further shows a power-law dependence on wind speed, with an exponent of approximately 2.31 and R^2=0.9704. The U-shaped response indicates that local peak erosion is more sensitive to spatial non-uniformity than the mean erosion. Yawed flow may normalize particle impacts within the windward region, increasing maximum erosion without a proportional increase in mean erosion.

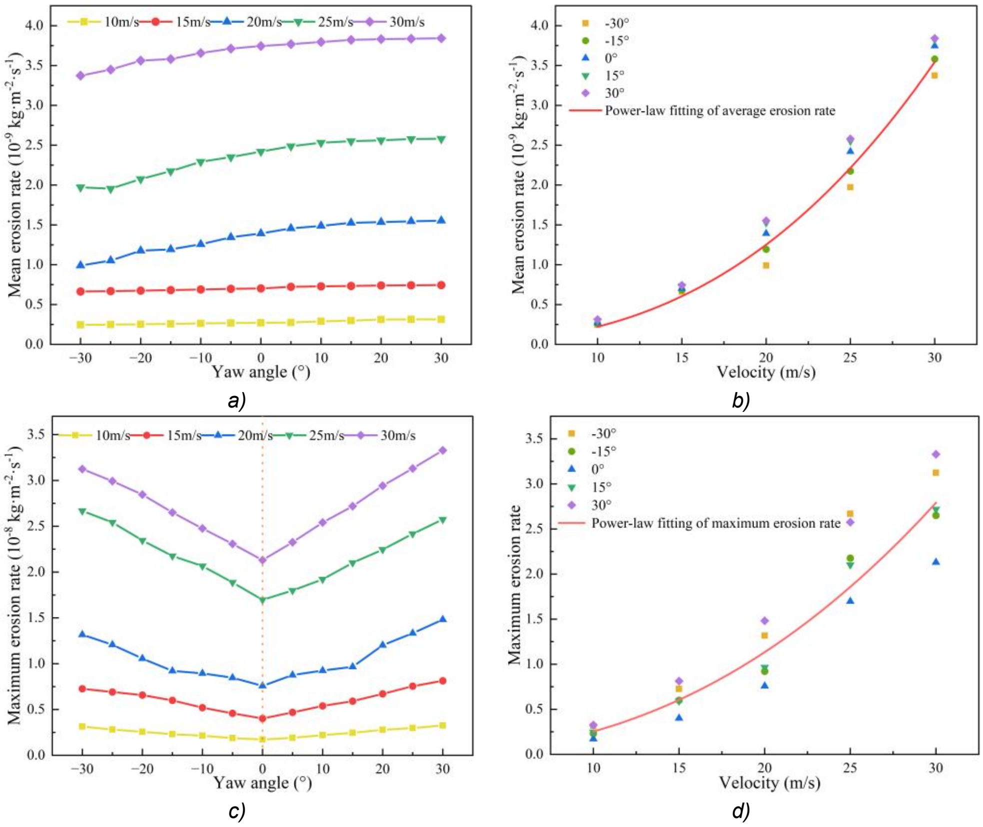

Fig. 5 – Erosion rate under different wind speeds and yaw angles

a) Mean erosion rate–yaw angle; b) Mean erosion rate–wind speed;
c) Maximum erosion rate–yaw angle; d) Maximum erosion rate–wind speed

To quantify the spatial concentration of erosion damage, the erosion concentration factor KCF was introduced as the ratio of the maximum erosion rate to the mean erosion rate:

$$KCF=\frac{E_{\max}}{E_{\text{avg}}} \tag{6}$$

where KCF is a dimensionless index describing the deviation of local peak erosion from the mean erosion level. $E_{\max}$ is the maximum erosion rate in the exposed region under the same condition, and E_{avg} is the corresponding mean erosion rate.

For clarity and to facilitate direct comparison with the experimental conditions, only the cases at 10, 20, and 30 m/s are presented in Figure 6. KCF was lowest near 0° and increased toward larger yaw angles; at 20 m/s, the values at −30°, 0°, and 30° were 13.31, 5.45, and 9.54, respectively. The variation in KCF primarily reflects changes in the spatial concentration of erosion rather than in the overall erosion intensity. Near 0°, particle impacts are distributed relatively broadly, reducing the difference between $E_{\max}$ and E_{avg}.

Under yawed conditions, asymmetric flow redistributes particle impacts and may increase their spatial concentration, causing the local peak to rise relative to the mean. This behaviour is physically analogous to the non-uniform particle-impact erosion discussed by *Hamed et al., (2006)*. Notably, the high KCF at −30°, despite a non-maximum E_{avg}, indicates that mean erosion alone may underestimate normalize damage. Therefore, E_{avg}, E_{max}, and KCF should be considered jointly to characterize both erosion severity and spatial concentration.

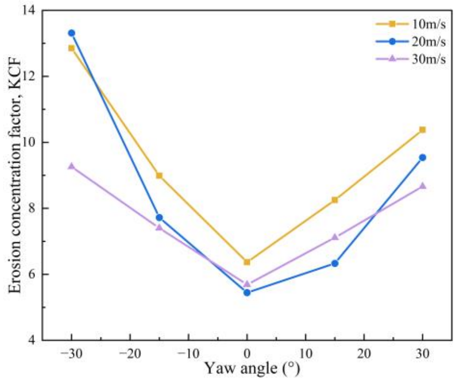

Fig. 6 – Variation of the KCF with yaw angle at different wind speeds

Erosion Damage and Surface Morphology Evolution of PC

Figure 7(a) shows that mass loss increased with both wind speed and yaw angle. From −30° to 30°, the mean mass loss increased by 212.5%, 115.4%, and 88.9% at 10, 20, and 30 m/s, respectively. The observed response is associated with changes in particle-impact momentum and incidence conditions. Higher wind speed increases particle momentum and impact energy, promoting local deformation and progressive material removal. Meanwhile, yaw modifies the relative normal and tangential impact components; the former favors indentation and deformation, whereas the latter promotes grooving and scratching. Their combined variation therefore alters the efficiency of material removal. In contrast, *Zhao et al., (2021),* reported a non-monotonic dependence of glass erosion on particle impact angle. This difference is physically reasonable because yaw angle is not equivalent to the local impact angle, which also depends on particle trajectory and surface orientation, while PC and glass exhibit different mechanical responses.

Surface roughness showed a similar overall trend in Figure 7(b). From −30° to 30°, the mean roughness increased from 5.82 to 7.21 μm, 6.67 to 7.93 μm, and 7.62 to 9.15 μm at 10, 20, and 30 m/s, representing increases of 23.9%, 18.9%, and 20.1%, respectively. The increase in surface roughness reflects the accumulation and overlap of pits, grooves, and displaced material. This result is similar to the deformation-related erosion response of polymeric materials discussed by Xie et al. (2019).

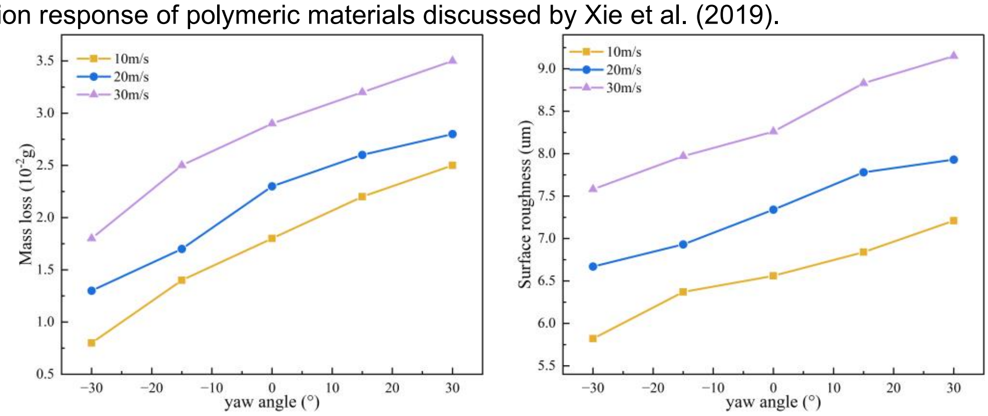

a) *b)*

Fig. 7 – Erosion characteristics of PC specimens

a) mass loss; b) surface roughness.

Figure 8 presents representative surface morphologies of PC specimens along a stepwise comparison path in which either yaw angle or wind speed was varied between adjacent conditions. At 10 m/s, increasing the yaw angle from −30° to −15° increased the density of isolated irregular defects, while relatively smooth regions remained visible. At a constant yaw angle of −15°, increasing the wind speed to 20 m/s enlarged the characteristic size of the defects and promoted local overlap. A further increase in yaw angle to 15° produced more densely distributed and partially interconnected damage features.

At the same yaw angle, increasing the wind speed to 30 m/s resulted in locally concentrated roughening, whereas increasing the yaw angle to 30° led to a more widespread and relatively continuous roughened surface. These changes are consistent with the increases in mass loss and surface roughness shown in Figure 7, indicating that enhanced material removal was accompanied by the accumulation, enlargement, and overlap of surface defects. Irregular local features may be associated with impact-induced deformation, while elongated and groove-like traces suggest the contribution of tangential abrasion. The observed surface degradation therefore reflects the combined effects of repeated particle impacts, local deformation, and abrasive material removal. The coexistence of impact-induced deformation and tangential abrasion is consistent with the combined deformation and cutting mechanisms reported in solid-particle erosion studies.

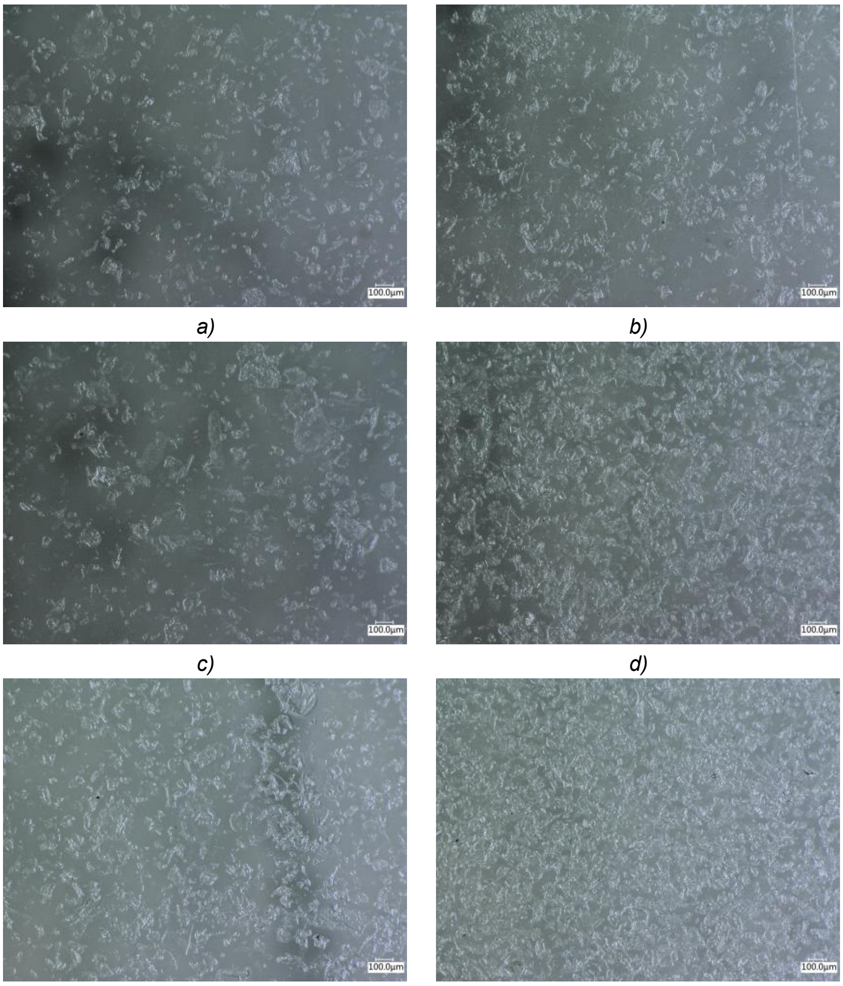

a) *b)* *c)* *d)* *e)* *f)*

Fig. 8 – Surface Damage and Morphology Variation of PC Specimens

a) $v = 10$ *m/s,* $\theta = -30°$; *b)* $v = 10$ *m/s,* $\theta = -15°$;
c) $v = 20$ *m/s,* $\theta = -15°$; *d)* $v = 20$ *m/s,* $\theta = 15°$;
e) $v = 30$ *m/s,* $\theta = 15°$; *f)* $v = 30$ *m/s,* $\theta = 30°$

Comparison between Numerical and Experimental Erosion Trends

To eliminate the difference in magnitude and units between the simulated mean erosion rate and the experimental mass loss, the two indicators were independently normalized within each wind-speed group using min–max normalization:

$$D_{i,j}^{*} = \frac{D_{i,j} - D_{min,j}}{D_{max,j} - D_{min,j}} \tag{7}$$

where $D_{i,j}^{*}$ is the normalized value of the i-th yaw-angle condition in the j-th wind-speed group; $D_{i,j}$ is the corresponding original value; and $D_{\min,j}$ and $D_{\max,j}$ are the minimum and maximum values of the same indicator within that wind-speed group, respectively. The simulated mean erosion rate and experimental mass loss were normalized separately using the same procedure. The resulting dimensionless indicators were used to compare their relative variations with yaw angle rather than their absolute magnitudes.

Figure 9(a) compares the normalized mean erosion rate with the normalized experimental mass loss. At all three wind speeds, both quantities generally increased as the yaw angle varied from −30° to 30°, indicating a consistent yaw-dependent response. This agreement can be attributed to the common dependence of both indicators on particle–surface interaction conditions. Variations in yaw alter the relative direction between the particle-laden flow and the exposed surface, thereby modifying particle trajectories, local incidence conditions, and the effective impact area. This result is similar to that reported by *Li et al. (2025)*, where numerical predictions and experimental measurements exhibited consistent variation trends in aeolian-particle transport. The remaining differences at intermediate yaw angles may be associated with the distinct geometrical and loading conditions of the two configurations of the two approaches: the simulation represents spatially averaged erosion over a curved lamp cover, whereas the experiment measures cumulative mass loss from a flat PC specimen subjected to jet impingement.

The correlation analysis in Figure 9(b) yielded R^2=0.9481, RMSE = 0.0822, and MAE = 0.0671, with most points distributed close to the 1:1 reference line. Because min–max normalization was performed separately within each wind-speed group, these statistics quantify similarity in the yaw-dependent variation rather than absolute predictive accuracy. The relatively high R^2 together with the low error metrics further indicate a consistent trend-level agreement between the numerical and experimental results, suggesting that both approaches capture the same variation pattern with respect to yaw angle.

The correlation analysis in Figure 9(b) yielded R^2=0.9481, RMSE = 0.0822, and MAE = 0.0671. Most data points were distributed near the 1:1 reference line, indicating close agreement between the relative variations of the numerical and experimental indicators. Because min–max normalization was performed independently within each wind-speed group, these statistics characterize similarity in the yaw-angle-dependent trends rather than absolute predictive accuracy. The high R^2 and relatively small errors therefore support trend-level agreement between the simulated mean erosion rate and experimental mass loss.

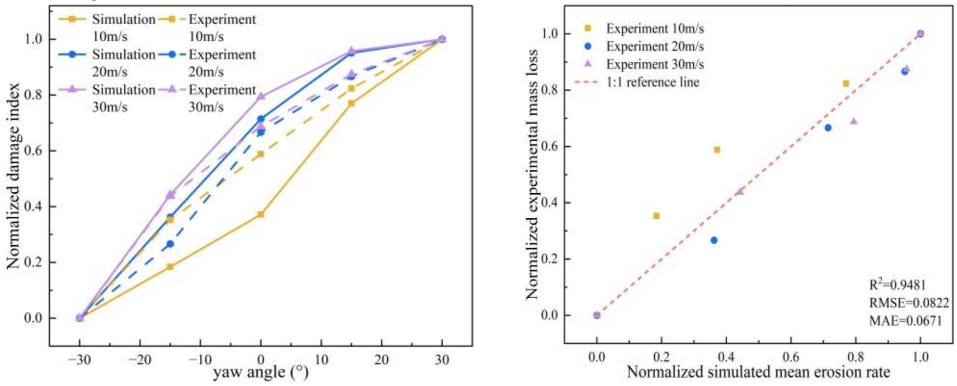

a) *b)*

Fig. 9 - Comparison between normalized numerical and experimental erosion indicators

a) Comparison of normalized simulation and experimental results;

b) Correlation between normalized simulation and experimental results

Fig.10 further quantifies the differences between the normalized numerical and experimental responses.

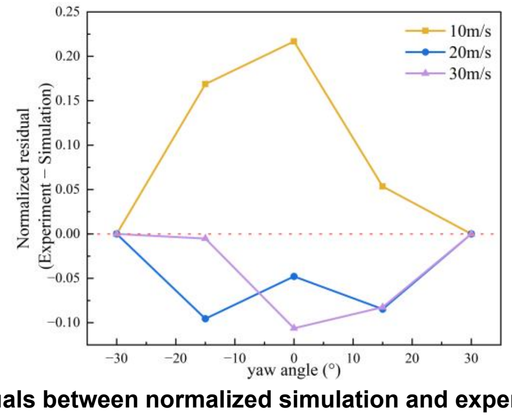

Fig. 10 - Residuals between normalized simulation and experimental results

Positive residuals occurred mainly at 10 m/s, indicating that the normalized experimental mass loss exceeded the corresponding normalized mean erosion rate at several intermediate yaw angles. At 20 and 30 m/s, negative residuals occurred more frequently at intermediate yaw angles, indicating comparatively higher normalized numerical values. This change in residual sign is likely related to differences in particle incidence, near-wall velocity, dispersion, and effective impact area between the curved lamp cover and the flat PC specimen. Despite these local deviations, both indicators retained the same overall yaw-dependent tendency. This result is similar in validation outcome to *Yan et al., (2024)*, whose wind-tunnel experiments supported the reliability of CFD predictions for wind–sand flow. The residual analysis therefore supports comparative evaluation of erosion response across wind-speed and yaw-angle conditions rather than direct prediction of experimental mass loss.

CONCLUSIONS

The wind-blown sand erosion characteristics of a PC lamp cover for agricultural machinery were investigated using one-way coupled Eulerian–Lagrangian simulations and controlled gas-jet erosion tests. The main conclusions were as follows:

(1) Erosion concentrated near the windward leading edge and adjacent downstream surface, whereas the leeward region was weakly affected. The pressure maximum occurred in the stagnation region, but the erosion maximum shifted downstream, suggesting that the spatial separation between the pressure and erosion maxima was associated with the combined effects of particle impact velocity, impact angle, local particle flux, and the near-wall flow field.

(2) Wind speed strongly influenced erosion intensity within the investigated range. Mean and maximum erosion rates followed power laws with exponents of approximately 2.70 and 2.31. As yaw changed from negative to positive values, the mean erosion rate generally increased, while the maximum erosion rate showed a U-shaped variation with a minimum near 0°.

(3) The erosion concentration factor KCF reflected localized damage. At 20 m/s, its values at −30°, 0°, and 30° were 13.31, 5.45, and 9.54, respectively. The high value at −30° showed that a relatively low mean erosion rate could coexist with pronounced local erosion concentration. Mean erosion rate, maximum erosion rate, and KCF should therefore be considered together.

(4) The coupon tests showed increasing mass loss and surface roughness with wind speed and yaw angle, accompanied by an increase in the density and coverage of surface defects. The normalized mean erosion rate followed the experimental mass-loss trend (R^2 = 0.9481, RMSE = 0.0822, MAE = 0.0671). Because the numerical and experimental configurations differed, this agreement supports relative trend prediction rather than absolute quantitative validation of the full-scale lamp-cover model.

ACKNOWLEDGEMENT

The authors were funded for this project by the National Natural Sciences Foundation of China (NSFC), Grant/Award Number: 12362033.

REFERENCES

[1] Alqallaf J., Ali N., Teixeira J.A., & Addali A. (2020). Solid particle erosion behaviour and protective coatings for gas turbine compressor blades—A review. *Processes*, 8(8), 984. https://doi.org/10.3390/pr8080984

[2] *** ASTM International. (2018). *ASTM G76-18: Standard test method for conducting erosion tests by solid particle impingement using gas jets*. ASTM International, West Conshohocken, Pennsylvania, USA. https://doi.org/10.1520/G0076-18

[3] Bellman R., & Levy A. (1981). Erosion mechanism in ductile metals. *Wear*, 70(1), 1–27. https://doi.org/10.1016/0043-1648(81)90268-4

[4] Bi H., Jia P., Qin K., Yu L., Cao C., Xia D., Guo X., Liu Y., Chen B., Bi Y. (2023). Porous hot air tea de-enzyming and carding machine under gas–solid coupling conditions: Numerical simulations and performance testing. *INMATEH – Agricultural Engineering*, 71(3), 301–318. https://doi.org/10.35633/inmateh-71-26

[5] Chen G., Li F., Qu F., & Zhang C. (2025). Simulation study on soybean winnowing based on CFD–DEM coupling. *INMATEH – Agricultural Engineering*, 77(3), 362–372. https://doi.org/10.35633/inmateh-77-29

[6] Deng T. (2025). Erosive wear mechanisms of materials—A review of understanding and progresses. *Materials*, 18(7), 1615. https://doi.org/10.3390/ma18071615

[7] Elghobashi S. (1994). On predicting particle-laden turbulent flows. *Applied Scientific Research*, 52(4), 309–329. https://doi.org/10.1007/BF00936835

[8] Ferreira M.M., & Lins V.F.C. (2019). Failure in automobile headlight lenses. *Engineering Failure Analysis*, 104, 844–855. https://doi.org/10.1016/j.engfailanal.2019.06.051

[9] Finnie I. (1960). Erosion of surfaces by solid particles. *Wear*, 3(2), 87–103. https://doi.org/10.1016/0043-1648(60)90055-7

[10] Hamed A., Tabakoff W., & Wenglarz R. (2006). Erosion and deposition in turbomachinery. *Journal of Propulsion and Power*, 22(2), 350–360. https://doi.org/10.2514/1.18462

[11] Hutchings I.M. (1981). A model for the erosion of metals by spherical particles at normal incidence. *Wear*, 70(3), 269–281. https://doi.org/10.1016/0043-1648(81)90347-1

[12] Katsamberis D., Browall K., Iacovangelo C., Neumann M., & Morgner H. (1998). Highly durable coatings for automotive polycarbonate glazing. *Progress in Organic Coatings*, 34(1–4), 130–134. https://doi.org/10.1016/S0300-9440(98)00002-2

[13] Kok J.F., Parteli E.J.R., Michaels T.I., & Bou Karam D. (2012). The physics of wind-blown sand and dust. *Reports on Progress in Physics*, 75(10), 106901. https://doi.org/10.1088/0034-4885/75/10/106901

[14] Li F., Jin A., Yang B., Li J., & Yang J. (2025). CFD–DEM simulation of aeolian sand transport: Effects of wind speed and sand particle shape. *INMATEH – Agricultural Engineering*, 77(3), 1116–1130. https://doi.org/10.35633/inmateh-77-90

[15] Menter F.R. (1994). Two-equation eddy-viscosity turbulence models for engineering applications. *AIAA Journal*, 32(8), 1598–1605. https://doi.org/10.2514/3.12149

[16] Oka Y.I., Ohnogi H., Hosokawa T., & Matsumura M. (1997). The impact angle dependence of erosion damage caused by solid particle impact. *Wear*, 203–204, 573–579. https://doi.org/10.1016/S0043-1648(96)07430-3

[17] Oka Y.I., Okamura K., & Yoshida T. (2005a). Practical estimation of erosion damage caused by solid particle impact: Part 1—Effects of impact parameters on a predictive equation. *Wear*, 259(1–6), 95–101. https://doi.org/10.1016/j.wear.2005.01.039

[18] Oka Y.I., & Yoshida T. (2005b). Practical estimation of erosion damage caused by solid particle impact: Part 2—Mechanical properties of materials directly associated with erosion damage. *Wear*, 259(1–6), 102–109. https://doi.org/10.1016/j.wear.2005.01.040

[19] Shao Y., & Lu H. (2000). A simple expression for wind erosion threshold friction velocity. *Journal of Geophysical Research: Atmospheres*, 105(D17), 22437–22443. https://doi.org/10.1029/2000JD900304

[20] Sundararajan G. (1991). A comprehensive model for the solid particle erosion of ductile materials. *Wear*, 149(1–2), 111–127. https://doi.org/10.1016/0043-1648(91)90368-5

[21] Wang J., Gao J., Zhang Y., & Cui H. (2024). Analysis of the sand erosion effect and wear mechanism of wind turbine blade coating. *Energies*, 17(2), 413. https://doi.org/10.3390/en17020413

[22] Xie Y., Jiang J.J., & Islam M.A. (2019). Elastomers and plastics for resisting erosion attack of abrasive/erosive slurries. *Wear*, 426–427, 612–619. https://doi.org/10.1016/j.wear.2019.01.123

[23] Yan M., Jin A., & Gao W. (2024). Optimization of joint sand barrier spacing and characterization of wind-sand flow study based on CFD numerical simulation. *INMATEH – Agricultural Engineering*, 73(2), 855–869. https://doi.org/10.35633/inmateh-73-72

[24] Zhang D.M., Huang Z.Y., Yi S.J., Wang S., & Chen Y.F. (2025). Simulation and experimental study on the stability of airflow distribution above the screen in an air-screen millet cleaning device. *INMATEH – Agricultural Engineering*, 77(3), 326–339. https://doi.org/10.35633/inmateh-77-26

[25] Zhao Y., Liu R., Yan F., Zhang D., & Liu J. (2021). Windblown sand-induced degradation of glass panels in curtain walls. *Materials*, 14(3), 607. https://doi.org/10.3390/ma14030607